Double Torsion Testing and Finite Element Analysis for Determining the Electric Fracture Properties of Piezoelectric Ceramics

doi: 10.1063/1.1925331

Double torsion testing and finite element analysis for determining the electric fracture properties of piezoelectric ceramics

Yasuhide Shindo,[a] Fumio Narita, and Masaru Mikami
Department of Materials Processing, Graduate School of Engineering, Tohoku University, Aoba-yama 6-6-02, Sendai 980-8579, Japan

(Received 28 October 2004; accepted 4 April 2005; published online 1 June 2005)

This paper presents the results of an experimental and numerical investigation in electric fracture behavior of composite $[Pb(Zr,Ti)O_3]$ double torsion (DT) specimens. DT tests were conducted on a commercial piezoelectric ceramic bonded between two metals. Fracture loads under different electric fields were obtained from the experiment. Nonlinear three-dimensional finite element analysis was also employed to calculate the energy release rate for DT specimens based on the exact (permeable) and approximate (impermeable) crack models. The effects of applied electric field and domain switching on the energy release rate are discussed, and the model predictions are compared with the results of the experiments. © *2005 American Institute of Physics*.
[DOI: 10.1063/1.1925331]

I. INTRODUCTION

$Pb(Zr,Ti)O_3$ (PZT) piezoceramics are candidates for use as sensor or actuator elements in biomaterials and microelectromechanical systems (MEMSs). In most of these applications the PZT ceramics are exposed to severe mechanical and electrical loading conditions which may result into structural failure or dielectric breakdown. Considerable researches have been theoretically devoted to fracture problems of PZT ceramics and composites under mechanical and electrical loads,[1–3] and experimental studies for cracks in various PZTs have been carried out. Park and Sun[4] performed mode I and mixed mode fracture tests on PZT piezoelectric ceramics, and showed that positive electric fields (electric fields in poling direction) aid crack propagation, while negative electric fields impede crack propagation. Shindo *et al.* also made indentation fracture (IF) tests with a load of 9.8 N on the PZT ceramics,[5] and employed a three-dimensional finite element analysis to calculate the fracture mechanics parameters such as total potential-energy release rate,[5] mechanical strain energy release rate, and energy density factor.[6] They obtained the experimental result consistent with that of Park and Sun.[4] The numerical results also showed that for a given load, positive electric fields increase the fracture mechanics parameters for the exact (permeable) crack model, while negative electric fields have an opposite effect, and agreed quantitatively with the experimental observations. However, the trend of the fracture mechanics parameters for the approximate (impermeable) crack model was not consistent with the experimental results.

On the other hand, Narita *et al.*[6] observed opposite phenomena in the crack growth in a PZT ceramic under electric fields from the single-edge precracked beam (SEPB) tests and corresponding finite element analysis. The results showed that for center-cracked piezoelectric specimens under three-point bending condition, positive electric fields increase the fracture deflection, and negative ones decrease it. The results of simulations based on the exact (permeable) crack model for applied displacement are consistent with these experimentally observed phenomena.[6,7] The numerical results for the exact (permeable) model under applied load are in contrast with those under a constant displacement, and agree with the three-point bending test results.[4]

As seen in the previous works, the influence of electric field on fracture behavior is different for each mechanical loading condition. Sun and Park[8] studied a method for determining the fracture toughness of PZT-4 piezoelectric ceramics using Vickers indentation with loads of 9.8 and 49 N. It was shown that for the indentation load of 9.8 N, experimental phenomena agree qualitatively with the observations in Refs. 4 and 5. For the 49-N load case, the trend is not similar to the 9.8-N load case for negative electric fields. Fu and Zhang[9] also conducted compact tension tests and IF tests with a load of 49 N to study the effects of applied electric fields on the fracture toughness of PZT ceramics, and showed that application of negative or positive electric fields reduces the apparent fracture toughness. A linear relationship between the fracture toughness and the applied electric field was not observed. Schneider and Heyer[10] investigated the crack growth in a ferroelectric barium titanate ($BaTiO_3$) ceramic under applied electric fields up to four times the coercive field strength by using the Vickers indentation technique. The peak indentation load of 40 N was applied. The curves of the measured crack length as a function of the applied electric field showed similarity with the strain hysteresis. Shindo *et al.*[11] investigated theoretically and experimentally the fracture and polarization properties of PZT ceramics under mechanical and electrical loads ultilizing the modified small punch test technique.

In this study, a theoretical and experimental investigation in electric fracture behavior of a piezoelectric ceramic was conducted. The DT tests were performed and the fracture loads were obtained for a composite PZT specimen. The electroelastic response of piezocomposite DT specimen under mechanical and electrical loads was also predicted using

[a]Electronic mail: shindo@material.tohoku.ac.jp

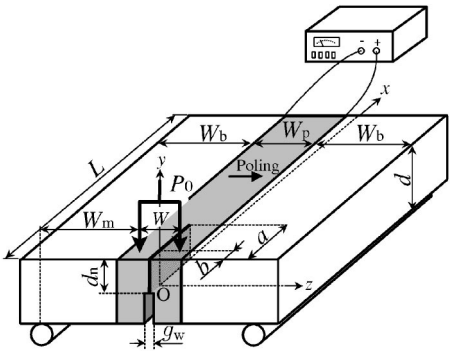

FIG. 1. Composite PZT double torsion specimen.

a nonlinear finite element approach, and the effect of electromechanical loading on the energy release rate for the exact (permeable) and approximate (impermeable) crack models was examined. Attempts are made to compare the results of finite element analysis with experimental observations.

II. EXPERIMENTAL PROCEDURE

The effect of applied electric field on fracture load in PZT ceramic was studied using the DT technique.[12] The specimen geometry used was a composite PZT DT specimen described by the Cartesian coordinate system (x,y,z), as shown in Fig. 1. The PZT samples of width $W_p=5$ mm, thickness $d=5$ mm, and length $L=30$ mm were cut. The specimen was produced by first poling a 5-mm-wide PZT beam and then bonding it between two wider brass beams of $W_b=7.5$ mm, $d=5$ mm, and $L=30$ mm with high strength epoxy. A side groove of depth $d-d_n=2.5$ mm and width $g_w=1$ mm was machined in the PZT. Before testing, a thin notch is cut in the end of the PZT to a depth of $d_n=2.5$ mm and a length of $a=5$ mm. The PZTs were commercially supplied P-7 (Murata Manufacturing Co., Ltd., Japan) and C-91 (Fuji Ceramics Co., Ltd., Japan). Material properties are listed in Table I and the coercive electric fields E_c of P-7 and C-91 are approximately 0.8 and 0.35 MV/m, respectively. Young's modulus and Poisson's ratio of brass are taken to be $E=100.6$ GPa and $\nu=0.35$.

The specimens were loaded by concentrated loads $P_0/2$ at $x=0$ mm, $y=2.5$ mm, and $z=\pm 2$ mm in a screw-driven testing machine. The moment arm W_m and distance b for our loading machine were fixed at 5.5 and 2 mm, respectively. To generate electric fields E_0, a power supply for voltages up to 1.25 kV/dc was used to apply a range of positive and negative electric fields of 0.25 MV/m. Loads which caused fracture were measured for each set of specimens for various electric fields.

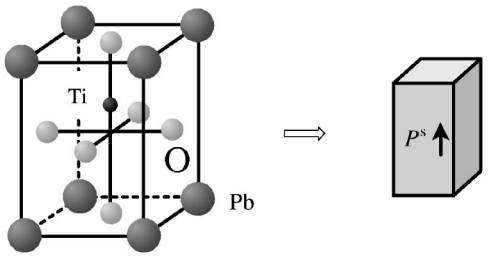

FIG. 2. Tetragonal crystal of lead titanate.

III. FINITE ELEMENT SOLUTION PROCEDURE

The most important class of ferroelectric materials is the perovskite oxides ABO_3 (e.g., $PbTiO_3$). Above the Curie temperature, the unit cell is the paraelectric simple cubic perovskite structure, with a Ti^{4+} ion at the cube center surrounded by six O^{2-} ions, and eight Pb^{2+} ions at the cube corners. As the temperature is reduced, a structural phase transition into a ferroelectric state takes place, in which the central Ti^{4+} ion displaces off-center with respect to the surrounding O^{2-} ions, so that the unit cell possesses a spontaneous polarization P^s and a spontaneous strain γ^s aligned with the dipole moment of the charge distribution (see Fig. 2).

A single crystal is comprised of many unit cells. A single crystal cooled below the Curie temperature contains many domains in which the electric dipole is aligned in a specific allowed direction. With the dipoles randomly oriented, the overall ceramic exhibits no piezoelectric effect. Piezoelectric behavior is induced by the poling process, that is, by applying a high voltage to the ceramic. The electric field aligns dipoles along the field lines. This alignment results in the remanent polarization, and the remanently polarized state has a remanent strain. Polarization switching occurs when an applied electric field exceeds the coercive field. In this section, a nonlinear finite element formulation is developed for piezoelectric ceramics.

A. Prediction of polarization switching

The governing field equations for a ferroelectric will be summarized. Equilibrium and Gauss' law are given by

$$\sigma_{ji,j}=0, \tag{1}$$

$$D_{i,i}=0, \tag{2}$$

where σ_{ij} and D_i are the stress and electric displacement, and a comma followed by an index denotes partial differentiation with respect to a space coordinate $x_i(i=1,2,3)$. We have em-

TABLE I. Material properties of the piezoelectric ceramics.

	Elastic stiffnesses ($\times 10^{10}$ N/m^2)					Piezoelectric coefficients (C/m^2)			Dielectric constants ($\times 10^{-10}$ C/Vm)	
	c_{11}	c_{33}	c_{44}	c_{12}	c_{13}	e_{31}	e_{33}	e_{15}	ϵ_{11}	ϵ_{33}
P-7	13.0	11.9	2.5	8.3	8.3	−10.3	14.7	13.5	171	186
C-91	12.0	11.4	2.4	7.7	7.7	−17.3	21.2	20.2	226	235

ployed Cartesian tensor notation and the summation convention for repeated tensor indices. The strain ε_{ij} and electric field E_i are

$$\varepsilon_{ij} = \tfrac{1}{2}(u_{j,i} + u_{i,j}), \tag{3}$$

$$E_i = -\phi_{,i}, \tag{4}$$

where u_i and ϕ are the displacement and electric potential, respectively. In a ferroelectric, domain-wall motion within each grain leads to a change in the remanent strain ε_{ij}^r and remanent polarization P_i^r. The total strain and electric displacement are described by

$$\varepsilon_{ij} = \varepsilon_{ij}^l + \varepsilon_{ij}^r, \tag{5}$$

$$D_i = D_i^l + P_i^r, \tag{6}$$

where the superscript l denotes the linear contribution to the strain and electric displacement, and the linear piezoelectric relationships are

$$\varepsilon_{ij}^l = s_{ijkl}\sigma_{kl} + d_{kij}E_k, \tag{7}$$

$$D_i^l = d_{ikl}\sigma_{kl} + \epsilon_{ik}E_k. \tag{8}$$

In Eqs. (7) and (8), s_{ijkl}, d_{kij}, and ϵ_{ik} are the elastic compliance, direct piezoelectric constant, and dielectric permittivity, which satisfy the following symmetry relations:

$$s_{ijkl} = s_{jikl} = s_{ijlk} = s_{jilk} = s_{klij}, \quad d_{kij} = d_{kji}, \quad \epsilon_{ik} = \epsilon_{ki}, \tag{9}$$

σ_{ij} and D_i^l are related to ε_{ij}^l and E_i by

$$\sigma_{ij} = c_{ijkl}\varepsilon_{kl}^l - e_{kij}E_k, \tag{10}$$

$$D_i^l = e_{ikl}\varepsilon_{kl}^l + \epsilon_{ik}E_k, \tag{11}$$

where c_{ijkl} and e_{ikl} are the elastic and piezoelectric constants, and

$$c_{ijkl} = c_{jikl} = c_{ijlk} = c_{jilk} = c_{klij}, \quad e_{kij} = e_{kji}. \tag{12}$$

The constitutive equations (10) and (11) for PZT poled in the x_3 direction are found in Appendix A.

The direction of P^s of each grain can change by 180° for ferroelectric switching induced by a sufficiently large electric field opposite to the poling direction. The 90° ferroelastic domain switching is induced by a sufficiently large stress field. Figure 3 illustrates several possibilities. The criterion states that a polarization switches when the electrical and mechanical work exceeds a critical value[13]

$$\sigma_{ij}\Delta\varepsilon_{ij} + E_i\Delta P_i \geqslant 2P^sE_c, \tag{13}$$

where $\Delta\varepsilon_{ij}$ and ΔP_i are the changes in the spontaneous strain and polarization during switching, respectively. The values of $\Delta\varepsilon_{ij}=\varepsilon_{ij}^r$ and $\Delta P_i=P_i^r$ are given in Appendix B for polarization switching in the x_3x_1 or x_2x_3 plane with x_3 as the original poling direction. The constitutive equations (10) and (11) during polarization switching are

$$\sigma_{ij} = c_{ijkl}\varepsilon_{kl}^l - e'_{kij}E_k, \tag{14}$$

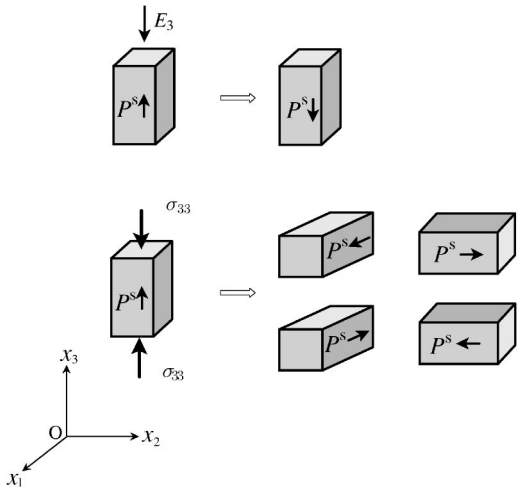

FIG. 3. 180° and 90° polarization switchings.

$$D_i^l = e'_{ikl}\varepsilon_{kl}^l + \epsilon_{ik}E_k. \tag{15}$$

The value of piezoelectric constant e'_{ikl} of each grain is given in Appendix C.

B. Energy release rate

Due to the polarization switching, piezoelectric media are often nonhomogeneous. The piezoelectric properties vary from one location to the other, and the variations are either continuous or discontinuous. Weichert and Schulz[14] proposed an extension of J integral to multiphase materials. The J integral for heterogeneous materials can be extended to piezoelectric crack problems. Figure 4 depicts a contour integral path including the bounded piezoelectric region. A local orthogonal coordinate system is defined at the crack tip such that x_1 and x_3 axes lie parallel and normal to the crack faces, respectively. The energy release rate G can be obtained from the following crack-tip integral:

$$G = \int_{\Gamma_0} (H\delta_{1j} - \sigma_{ij}u_{i,1} + D_jE_1)n_j d\Gamma - \int_{\Gamma_p} (H\delta_{1j} - \sigma_{ij}u_{i,1} + D_jE_1)n_j d\Gamma, \tag{16}$$

where Γ_0 is a small contour closing a crack tip, Γ_p is a path embracing that part of phase boundary which is enclosed by Γ_0, δ_{ij} is Kronecker delta, and n_j is the unit normal vector.

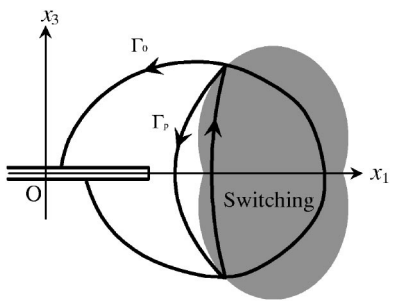

FIG. 4. Contours for the path-independent integrals.

The electrical enthalpy density is expressed as

$$H = \tfrac{1}{2} c_{ijkl}\varepsilon_{ij}\varepsilon_{kl} - \tfrac{1}{2}\epsilon_{ij}E_iE_j - e_{ikl}\varepsilon_{kl}E_i. \tag{17}$$

C. Analysis

Three-dimensional finite element calculations were made to determine the fracture mechanics parameters for the composite DT specimens shown in Fig. 1. A mechanical load was produced by the application of a prescribed force $P_0/2$ at $x=0$, $y=d_n$, and $z=\pm W/2$. For electrical loads, a positive or negative electric potential $\phi_0=-(W_p/2)E_0$ was applied at the interface, $-b\leqslant x\leqslant L-b$, $-(d-d_n)\leqslant y\leqslant d_n$, $z=W_p/2$. The interface $-b\leqslant x\leqslant L-b$, $-(d-d_n)\leqslant y\leqslant d_n$, $z=-W_p/2$ is grounded. If the crack faces are perpendicular to the poling direction and the electric field resulting from the application of ϕ_0 is oriented perpendicular to the crack, we have a mode I problem. Because of symmetry, only the right half of the model was used in the finite element analysis.

The crack faces are stress-free, and the crack face electrical boundary conditions are

$$\begin{aligned}
&E_x(x,y,0) = E_x^c(x,y,0) \quad (-b\leqslant x<a-b, \quad 0\leqslant y\leqslant d_n),\\
&E_y(x,y,0) = E_y^c(x,y,0) \quad (-b\leqslant x<a-b, \quad 0\leqslant y\leqslant d_n),\\
&\phi(x,y,0) = 0 \quad (a-b\leqslant x\leqslant L-b, \quad 0\leqslant y\leqslant d_n),\\
&D_z(x,y,0) = D_z^c(x,y,0) \quad (-b\leqslant x<a-b, \quad 0\leqslant y\leqslant d_n),
\end{aligned} \tag{18, 19}$$

where the superscript c stands for the electric-field quantity in the void inside the crack. The electric potential is all zero on the symmetry planes inside the crack and ahead of the crack, so the boundary conditions of Eqs. (18) reduce to $\phi(x,y,0)=0(-b\leqslant x\leqslant L-b, 0\leqslant y\leqslant d_n)$. The electric-field intensities $E_x^c(x,y,0)$ and $E_y^c(x,y,0)$ are equal to zero, and the electric displacement $D_z^c(x,y,0)$ is determined precisely. The loading conditions can be written as

$$\sigma_{yy}(x,d_n,z) = -(P_0/2)\delta(x)\delta(z-W/2), \tag{20}$$

$$\phi(x,y,W_p/2) = \phi_0/2 \qquad [-b\leqslant x\leqslant L-b, \quad -(d-d_n)\leqslant y\leqslant d_n], \tag{21}$$

where $\delta(\ )$ is the Dirac-delta function. Equations (18) and (19) are the exact (permeable) boundary conditions. On the other hand, the approximate (impermeable) boundary condition is

$$\begin{aligned}
&D_z(x,y,0) = 0 \quad (-b\leqslant x<a-b, \quad 0\leqslant y\leqslant d_n),\\
&\phi(x,y,0) = 0 \quad (a-b\leqslant x\leqslant L-b, \quad 0\leqslant y\leqslant d_n).
\end{aligned} \tag{22}$$

In electrostatics, at a surface separating two dielectric bodies, the normal component of the electric displacement and the tangential component of the electric field are continuous. However, when one of the bodies is air, these two conditions can be approximated simply by one, namely, that the normal component of the electric displacement vanishes at the interface. This impermeable assumption is based on the fact that there is a very large difference between the dielectric constants of the body and the air. When a spherical or a spheroidal defect problem in piezoelectric ceramics is analyzed, the impermeable condition is a good approximation. The electroelastic fields around a defect for the impermeable model, however, are quite different from those for the permeable model when the defect becomes a sharp notch or a crack.[6] The permeable model provides predictions of fracture properties due to electromechanical loading and better qualitative agreement with the experimental results,[5–7] and is appropriate for a crack in piezoelectric ceramics.

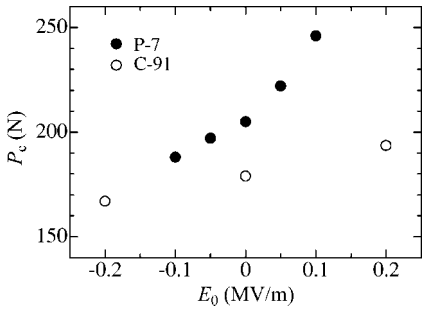

FIG. 5. Fracture load vs electric field.

Each element consists of many grains, and each grain is modeled as a uniformly polarized cell that contains a single domain. The model neglects the domain-wall effects and interaction among different domains. In reality, this is not true, but the assumption does not affect the general conclusions drawn. The polarization of each grain initially aligns as closely as possible with the z direction. The polarization switching is defined for each element in a material. Boundary loads are applied, and the electroelastic fields of each element are computed from the finite element analysis. Inhomogeneities in the local electroelastic fields and the effects of the grain size and orientation are ignored so that each grain is subjected to the same loading conditions. The switching criterion of Eq. (13) is checked for every element to see if switching will occur. After all possible polarization switches have occurred, the piezoelectric tensor of each element is rotated to the new polarization direction. The electroelastic fields are recalculated, and the process is repeated until the solution converges. The macroscopic response of the material is determined by the finite element model, which is an aggregate of elements. The spontaneous polarization P^s and strain γ^s are assigned representative values of 0.3 $\mathrm{C/m^2}$ and 0.004, respectively. Our previous experiments[15–17] verified the accuracy of the above scheme, and showed that the results obtained are of general applicability.

IV. RESULTS AND DISCUSSION

Figure 5 shows the measured fracture loads P_c of P-7 and C-91 for the crack length $a=5$ mm under various values of applied electric field E_0. A positive electric field increases the fracture load, and a negative one decreases it. Hence, the crack opens less under a positive electric field than under a negative electric field. These experimentally observed phenomena contradict the results of three-point bending[4] and IF

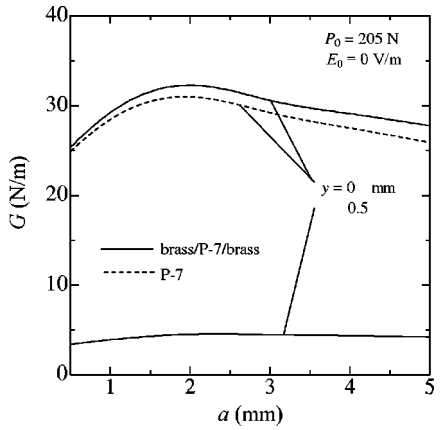

FIG. 6. Energy release rate vs crack length.

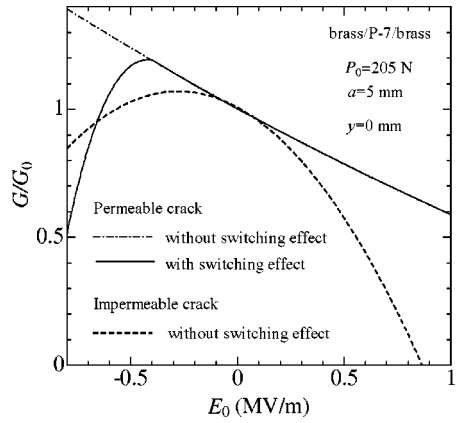

FIG. 8. Energy release rate vs electric field with switching effect.

(Ref. 5) tests. It is suggested that the negative electric field puts the DT specimen under tension (near the crack tip) and the positive electric field exerts a compressive stress (near the crack tip). The growth mechanism for a crack in the DT specimen is quite different from that in the conventional fracture tests with SEPB and Vickers' indentation specimens. The fracture loads depend on the material properties.

Figure 6 gives a plot of the energy release rate G versus crack length a for brass/P-7/brass at $y=0$ and 0.5 mm under $P_0=205$ N and $E_0=0$ V/m. Also shown is the energy release rate for P-7 ($W_p=20$ mm, $d=5$ mm, and $L=30$ mm) without brass at $y=0$ mm. The magnitude of G increases with a reaching a maximum value and then decreases. The G is largest on the $y=0$-mm plane. Figure 7 shows the energy release rate G for the permeable crack of $a=5$ mm under $P_0=205$ N with E_0 divided by G_0 at the same load but without the electric field. Results are also plotted for the impermeable crack model. For a given load, positive E_0 decreases the energy release rate for the permeable crack, while negative E_0 has an opposite effect. The increase in P_c with increasing positive E_0 is attributed to the decrease of G with increasing positive E_0 under a constant load P_0. Numerical results for the permeable crack under a constant load are in contrast with those for SEPB (Ref. 7) and IF (Ref. 6) tests under a constant load. In the impermeable case, the energy release rate G^I first increases up to a maximum value for a certain negative E_0, and then it begins to decrease for larger negative electric fields. On the other hand, as the magnitude of positive E_0 is increased from zero, the energy release rate G^I can be made to decrease. When a positive or negative E_0 is larger, a negative G^I is produced. It has been pointed out previously (e.g., Refs. 2 and 3). The energy release rate for the impermeable crack model has questionable physical significance. Figure 8 shows the dependence of G for the permeable crack model without and with switching effect under $P_0=205$ N on E_0 for $a=5$ mm, normalized by values for $E_0=0$ V/m. Also shown is the result for the impermeable crack model without switching effect. A monotonically increasing negative E_0 causes polarization switching. After E_0 reaches about -0.4 MV/m, polarization switching in a local region leads to an unexpected decrease in G for the permeable crack. Our previous experimental study[11] showed a significant nonlinearity in the fracture load due to polarization switching. The nonlinear effect caused by polarization switching may affect the piezoelectric crack behavior.

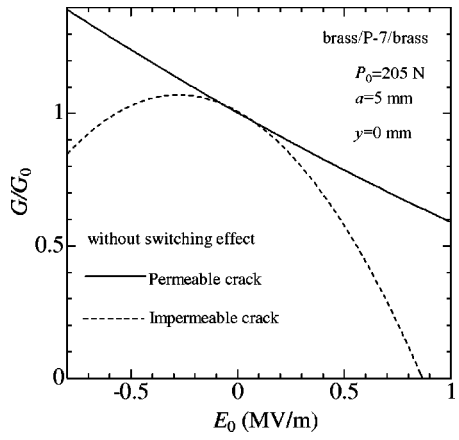

FIG. 7. Energy release rate vs electric field without switching effect.

V. CONCLUSIONS

The fracture behavior of piezoelectric ceramics was investigated under mechanical and electrical loads utilizing the DT technique. The magnitude as well as the direction of the applied electric field was found to have a significant influence on fracture load and energy release rate. Based on the experimental and numerical results for the piezoelectric composite DT specimen, the following conclusions may be inferred:

(1) A negative electric field decreases the fracture load, whereas a positive electric field increases it.
(2) At low electric-field levels, the energy release rate for the permeable crack model under negative electric field is higher in magnitude than those under positive electric fields. An increasing negative electric field causes polarization reversal, and polarization switching in a local region leads to a decrease of energy release rate.
(3) Increasing negative and positive electric fields lead to a negative-energy release rate for the impermeable crack model, and therefore the fracture criteria for the impermeable crack model are unreliable.

ACKNOWLEDGMENTS

This work was supported by the Ministry of Education, Culture, Sports, Science and Technology of Japan under the Grant-in-Aid for Scientific Research (B).

APPENDIX A

For piezoceramics which exhibit symmetry of a hexagonal crystal of class 6 mm with respect to principal x_1, x_2, and x_3 axes, the constitutive relations can be written in the following form:

$$\begin{Bmatrix} \sigma_1 \\ \sigma_2 \\ \sigma_3 \\ \sigma_4 \\ \sigma_5 \\ \sigma_6 \end{Bmatrix} = \begin{bmatrix} c_{11} & c_{12} & c_{13} & 0 & 0 & 0 \\ c_{12} & c_{11} & c_{13} & 0 & 0 & 0 \\ c_{13} & c_{13} & c_{33} & 0 & 0 & 0 \\ 0 & 0 & 0 & c_{44} & 0 & 0 \\ 0 & 0 & 0 & 0 & c_{44} & 0 \\ 0 & 0 & 0 & 0 & 0 & c_{66} \end{bmatrix} \begin{Bmatrix} \varepsilon_1^l \\ \varepsilon_2^l \\ \varepsilon_3^l \\ \varepsilon_4^l \\ \varepsilon_5^l \\ \varepsilon_6^l \end{Bmatrix} - \begin{bmatrix} 0 & 0 & e_{31} \\ 0 & 0 & e_{31} \\ 0 & 0 & e_{33} \\ 0 & e_{15} & 0 \\ e_{15} & 0 & 0 \\ 0 & 0 & 0 \end{bmatrix} \begin{Bmatrix} E_1 \\ E_2 \\ E_3 \end{Bmatrix}, \tag{A1}$$

$$\begin{Bmatrix} D_1^l \\ D_2^l \\ D_3^l \end{Bmatrix} = \begin{bmatrix} 0 & 0 & 0 & 0 & e_{15} & 0 \\ 0 & 0 & 0 & e_{15} & 0 & 0 \\ e_{31} & e_{31} & e_{33} & 0 & 0 & 0 \end{bmatrix} \begin{Bmatrix} \varepsilon_1^l \\ \varepsilon_2^l \\ \varepsilon_3^l \\ \varepsilon_4^l \\ \varepsilon_5^l \\ \varepsilon_6^l \end{Bmatrix} + \begin{bmatrix} \epsilon_{11} & 0 & 0 \\ 0 & \epsilon_{11} & 0 \\ 0 & 0 & \epsilon_{33} \end{bmatrix} \begin{Bmatrix} E_1 \\ E_2 \\ E_3 \end{Bmatrix}, \tag{A2}$$

where

$$\begin{matrix} \sigma_1 = \sigma_{11}, & \sigma_2 = \sigma_{22}, & \sigma_3 = \sigma_{33} \\ \sigma_4 = \sigma_{23} = \sigma_{32}, & \sigma_5 = \sigma_{31} = \sigma_{13}, & \sigma_6 = \sigma_{12} = \sigma_{21} \end{matrix}, \tag{A3}$$

$$\begin{matrix} \varepsilon_1^l = \varepsilon_{11}^l, & \varepsilon_2^l = \varepsilon_{22}^l, & \varepsilon_3^l = \varepsilon_{33}^l \\ \varepsilon_4^l = 2\varepsilon_{23}^l = 2\varepsilon_{32}^l, & \varepsilon_5^l = 2\varepsilon_{31}^l = 2\varepsilon_{13}^l, & \varepsilon_6^l = 2\varepsilon_{12}^l = 2\varepsilon_{21}^l \end{matrix}, \tag{A4}$$

$$c_{11} = c_{1111} = c_{2222}, \quad c_{12} = c_{1122}, \quad c_{13} = c_{1133} = c_{2233},$$

$$c_{33} = c_{3333} \qquad c_{44} = c_{2323} = c_{3131}, \tag{A5}$$

$$c_{66} = c_{1212} = \tfrac{1}{2}(c_{11} - c_{12}),$$

$$e_{15} = e_{131} = e_{223}, \quad e_{31} = e_{311} = e_{322}, \quad e_{33} = e_{333}. \tag{A6}$$

APPENDIX B

The values in $\Delta\varepsilon_{ij} = \varepsilon_{ij}^r$ and $\Delta P_i = P_i^r$ for 180° switching can be expressed as

$$\Delta\varepsilon_{11} = 0, \quad \Delta\varepsilon_{22} = 0, \quad \Delta\varepsilon_{33} = 0, \quad \Delta\varepsilon_{12} = 0,$$
$$\Delta\varepsilon_{23} = 0, \quad \Delta\varepsilon_{31} = 0, \tag{B1}$$

$$\Delta P_1 = 0, \quad \Delta P_2 = 0, \quad \Delta P_3 = -2P^s. \tag{B2}$$

For 90° switching in the x_3x_1 plane, there results

$$\Delta\varepsilon_{11} = \gamma^s, \quad \Delta\varepsilon_{22} = 0, \quad \Delta\varepsilon_{33} = -\gamma^s, \quad \Delta\varepsilon_{12} = 0,$$
$$\Delta\varepsilon_{23} = 0, \quad \Delta\varepsilon_{31} = 0, \tag{B3}$$

$$\Delta P_1 = \pm P^s, \quad \Delta P_2 = 0, \quad \Delta P_3 = -P^s. \tag{B4}$$

For 90° switching in the x_2x_3 plane,

$$\Delta\varepsilon_{11} = 0, \quad \Delta\varepsilon_{22} = \gamma^s, \quad \Delta\varepsilon_{33} = -\gamma^s, \quad \Delta\varepsilon_{12} = 0,$$
$$\Delta\varepsilon_{23} = 0, \quad \Delta\varepsilon_{31} = 0, \tag{B5}$$

$$\Delta P_1 = 0, \quad \Delta P_2 = \pm P^s, \quad \Delta P_3 = -P^s. \tag{B6}$$

APPENDIX C

The new piezoelectric constant e'_{ikl} is related to the elastic and direct piezoelectric constants by

$$e'_{111} = d'_{111}c_{11} + d'_{122}c_{12} + d'_{133}c_{13},$$
$$e'_{122} = d'_{111}c_{12} + d'_{122}c_{11} + d'_{133}c_{13},$$
$$e'_{133} = d'_{111}c_{13} + d'_{122}c_{13} + d'_{133}c_{33},$$
$$e'_{123} = 2d'_{123}c_{44},$$
$$e'_{131} = 2d'_{131}c_{44},$$
$$e'_{112} = 2d'_{112}c_{66},$$
$$e'_{211} = d'_{211}c_{11} + d'_{222}c_{12} + d'_{233}c_{13},$$
$$e'_{222} = d'_{211}c_{12} + d'_{222}c_{11} + d'_{233}c_{13},$$
$$e'_{233} = d'_{211}c_{13} + d'_{222}c_{13} + d'_{233}c_{33},$$
$$e'_{223} = 2d'_{223}c_{44},$$
$$e'_{231} = 2d'_{231}c_{44},$$
$$e'_{212} = 2d'_{212}c_{66},$$
$$e'_{311} = d'_{311}c_{11} + d'_{322}c_{12} + d'_{333}c_{13},$$
$$e'_{322} = d'_{311}c_{12} + d'_{322}c_{11} + d'_{333}c_{13},$$
$$e'_{333} = d'_{311}c_{13} + d'_{322}c_{13} + d'_{333}c_{33},$$

$$e'_{323} = 2d'_{323}c_{44},$$

$$e'_{331} = 2d'_{331}c_{44},$$

$$e'_{312} = 2d'_{312}c_{66}. \tag{C1}$$

The components of the piezoelectric tensor d'_{ikl} are

$$d'_{ikl} = \{d_{33}n_in_kn_l + d_{31}(n_i\delta_{il} - n_in_kn_l) + \tfrac{1}{2}d_{15}(\delta_{ik}n_l - 2n_in_kn_l + \delta_{il}n_k)\}, \tag{C2}$$

where n_i is the unit vector in the poling direction, δ_{ij} is the Kronecker delta, and $d_{33}=d_{333}$, $d_{31}=d_{311}$, $d_{15}=2d_{131}$ are the direct piezoelectric constants.

[1]F. Narita and Y. Shindo, Theor. Appl. Fract. Mech. **36**, 73 (2001).
[2]S. Lin, F. Narita, and Y. Shindo, Theor. Appl. Fract. Mech. **39**, 229 (2003).
[3]S. Lin, F. Narita, and Y. Shindo, Int. J. Solids Struct. **40**, 5157 (2003).
[4]S. Park and C. T. Sun, J. Am. Ceram. Soc. **78**, 1475 (1995).
[5]Y. Shindo, M. Oka, and K. Horiguchi, ASME J. Eng. Mater. Technol. **123**, 293 (2001).
[6]F. Narita, Y. Shindo, and K. Horiguchi, *Mechanics of Electromagnetic Material Systems and Structures* (WIT, Southampton, UK, 2003), p. 89.
[7]Y. Shindo, H. Murakami, K. Horiguchi, and F. Narita, J. Am. Ceram. Soc. **85**, 1243 (2002).
[8]C. T. Sun and S. B. Park, Ferroelectrics **248**, 79 (2000).
[9]R. Fu and T. Y. Zhang, J. Am. Ceram. Soc. **83**, 1215 (2000).
[10]G. A. Schneider and V. Heye, J. Eur. Ceram. Soc. **19**, 1299 (1999).
[11]Y. Shindo, F. Narita, K. Horiguchi, Y. Magara, and M. Yoshida, Acta Mater. **51**, 4773 (2003).
[12]A. G. Evans, J. Mater. Sci. **7**, 1137 (1972).
[13]S. C. Hwang, C. S. Lynch, and R. M. McMeeking, Acta Metall. Mater. **43**, 2073 (1995).
[14]D. Weichert and M. Schulz, Comput. Mater. Sci. **1**, 241 (1993).
[15]K. Hayashi, Y. Shindo, and F. Narita, J. Appl. Phys. **94**, 4603 (2003).
[16]M. Yoshida, F. Narita, Y. Shindo, M. Karaiwa, and K. Horiguchi, Smart Mater. Struct. **12**, 972 (2003).
[17]Y. Shindo, M. Yoshida, F. Narita, and K. Horiguchi, J. Mech. Phys. Solids **52**, 1109 (2004).